

# Global Learnable Attention for Single Image Super-Resolution

Jian-Nan Su, Min Gan\*, *Senior Member, IEEE*, Guang-Yong Chen, Jia-Li Yin,  
and C. L. Philip Chen, *Fellow, IEEE*

**Abstract**—Self-similarity is valuable to the exploration of non-local textures in single image super-resolution (SISR). Researchers usually assume that the importance of non-local textures is positively related to their similarity scores. In this paper, we surprisingly found that when repairing severely damaged query textures, some non-local textures with low-similarity which are closer to the target can provide more accurate and richer details than the high-similarity ones. In these cases, low-similarity does not mean inferior but is usually caused by different scales or orientations. Utilizing this finding, we proposed a Global Learnable Attention (GLA) to adaptively modify similarity scores of non-local textures during training instead of only using a fixed similarity scoring function such as the dot product. The proposed GLA can explore non-local textures with low-similarity but more accurate details to repair severely damaged textures. Furthermore, we propose to adopt Super-Bit Locality-Sensitive Hashing (SB-LSH) as a preprocessing method for our GLA. With the SB-LSH, the computational complexity of our GLA is reduced from quadratic to asymptotic linear with respect to the image size. In addition, the proposed GLA can be integrated into existing deep SISR models as an efficient general building block. Based on the GLA, we constructed a Deep Learnable Similarity Network (DLSN), which achieves state-of-the-art performance for SISR tasks of different degradation types (e.g. blur and noise). Our code and a pre-trained DLSN have been uploaded to GitHub<sup>†</sup> for validation.

**Index Terms**—Self-Similarity, Single Image Super-Resolution, Non-Local Attention, Deep Learning.

## 1 INTRODUCTION

SINGLE Image Super-Resolution (SISR) aims to recover a high-resolution (HR) image from its low-resolution (LR) input image, and it is useful in many important applications, such as medical imaging and object detection [8], [31]. Formally, the degradation process of the HR image can be defined as

$$\mathbf{I} = \mathbf{D}(\mathbf{H}; \beta), \quad (1)$$

where  $\mathbf{I} \in R^{h \times w}$  is an observed LR image and  $\mathbf{H} \in R^{sh \times sw}$  is a corresponding HR image.  $s$  is a down-scaling factor.  $\mathbf{D}(\cdot)$  denotes the degradation operation with parameters  $\beta$  and the default choice for  $\mathbf{D}(\cdot)$  in previous researches [4], [11], [20], [25] is the bicubic downsampling operator. If we consider the degradation under non-ideal conditions (e.g. blurring and additive noise), which is closer to the real-world scenario, the degradation can be generalized as follows

$$\mathbf{I} = \mathbf{D}(\mathbf{k} * \mathbf{H}; \beta) + \mathbf{n}, \quad (2)$$

where  $*$  denotes the convolution operation,  $\mathbf{k}$  is a blur kernel with low pass filter, and  $\mathbf{n}$  is an additive noise.

The SISR tasks, recovering  $\mathbf{H}$  from  $\mathbf{I}$ , are regarded as severely ill-posed problems, particularly when the scaling

factor is large. To generate visually pleasing results, it is common practice to use natural image priors such as the representative self-similarity. Thus, many self-similarity-based SISR methods [5], [7], [11], [25], [26] were proposed to address the ill-posedness and achieved satisfactory reconstruction results. The self-similarity is based on an observation that small textures in a natural image tend to recur within and across scales of the image [7], [43]. These repeated textures can provide valuable internal examples for a more faithful reconstruction. Essentially, the self-similarity provides valuable priors for exploring non-local image information. For example, when repairing hair textures, the related non-local hair regions are obviously more meaningful than low-frequency face regions or structured architectural regions. However, in SISR problems, previous studies usually assumed that the importance of non-local textures is positively related to their similarity scores, ignoring the flaws of this assumption, i.e., non-local textures with low-similarity may provide more accurate and richer details than the ones with high-similarity, especially when the query textures are severely damaged.

In this paper, we seek a deeper understanding of the role that the self-similarity plays in SISR tasks and expand its applicability in deep SISR models. In existing deep SISR models, the self-similarity is often integrated by non-local attention (NLA) [34], which was first proposed to explicitly model the long-range feature dependencies for high-level computer vision and also proven to be effective in SISR [3], [21], [26]. These NLA-based SISR models achieved satisfactory reconstruction performance by utilizing the NLA to capture the self-similarity priors. However, the previous methods are all based on a basic assumption to explore the self-similarity: *non-local textures that are more similar to the*

- \* Corresponding author (E-mail: [aganmin@aliyun.com](mailto:aganmin@aliyun.com))
- † <https://github.com/laoyangui/DLSN>
- Jian-Nan Su, Min Gan, Guang-Yong Chen and Jia-Li Yin are with the College of Computer and Data Science, Fuzhou University, Fuzhou 350108, China.
- C. L. Philip Chen is with the School of Computer Science and Engineering, South China University of Technology, Guangzhou 510641, China, and also with the Faculty of Science and Technology, University of Macau, Macau, China

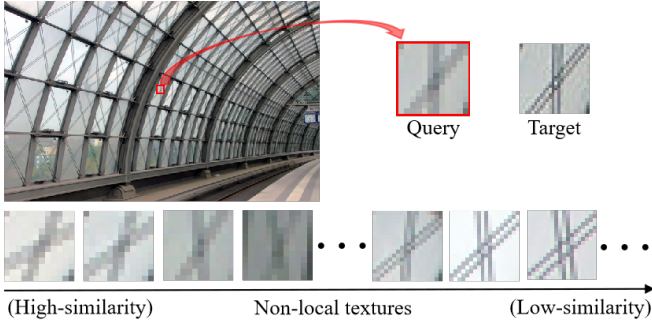


Fig. 1: An illustration of the similarity-based non-local textures exploration. Non-local textures with low-similarity can provide more accurate details for SR reconstruction, especially when the query textures are severely damaged.

*query textures can provide richer information.* We argue that the basic assumption is not always valid for SISR tasks. As illustrated in Fig. 1, when a similarity-based non-local search is performed on the severely damaged query textures, non-local textures with high-similarity will get higher similarity scores. However, these high-similarity non-local textures obviously cannot provide the critical information for repairing the severely damaged query textures. Essentially, the reason for this defect is that the basic assumption of the self-similarity cannot handle the situation where low-similarity textures are more accurate and informative than high-similarity textures. Repairing such severely damaged textures is a critical and extremely difficult task for SISR, so it is meaningful to design a non-local textures exploration scheme that can handle this situation. Another problem of NLA-based SISR models is that the computational complexity is quadratic to the size of the input image, which is generally unacceptable for SISR tasks.

To address these issues, we proposed a Global Learnable Attention (GLA) module, which can modify similarity score between two features adaptively during training and has asymptotic linear computational complexity with respect to the size of the input image. Our GLA module consists of two core parts: a Learnable Similarity Scoring (LSS) function and a Super-Bit Locality-Sensitive Hashing (SB-LSH) [12]. With the SB-LSH, our GLA module can perform hashing on input features and compute similarity only within the same hash bucket. The SB-LSH not only can reduce the computational complexity of the standard self-attention from quadratic to asymptotic linear, but also eliminate a large amount of redundant and irrelevant non-local information. The proposed LSS function aims to address the inherent limitations of the self-similarity (see Fig. 1) by providing trainable parameters to adaptively modify similarity scores between input features. Furthermore, we constructed a Global Learnable Attention based Features Fusion Module (GLAFFM) to fuse local adjacency information and learnable non-local self-similarity information. The local adjacency information is captured by the common component of Local Features Fusion Block (LFFB) that consists of several simple residual convolution layers. Finally, we integrated some GLAFFMs into a residual backbone to build our Deep Learnable Similarity Network (DLSN) (see Fig. 2) for SISR tasks.

The effectiveness of our DLSN will be verified in

the experiment section for different degradation types of SISR tasks: bicubic-downscale, blur-downscale, and noisy-downscale. In all degradation types, our DLSN outperforms other state-of-the-art SISR models [3], [26], [40], [41] by a large margin. In addition, to verify the universality of our GLA in deep SISR, we integrated our GLA into some representative deep SISR models, such as FSRCNN [4], EDSR [20], and RCAN [40]. Experimental results demonstrate that our GLA can significantly improve the SR performance of various deep SISR models. Ablation studies are also conducted to analyze the impact of the proposed LFFB and GLA on the reconstruction results.

The main contributions of this paper are summarized as follows.

- We provide some new insights into the self-similarity-based SISR solutions and argue that the basic assumption of the self-similarity is not flexible enough for SISR tasks. (As shown in Fig. 1)
- The proposed Global Learnable Attention (GLA) with Super-Bit Locality-Sensitive Hashing (SB-LSH) can adaptively modify the similarity scores during training and has asymptotic linear computational complexity.
- A new Deep Learnable Similarity Network (DLSN) is designed by using our Global Learnable Attention-based Features Fusion Modules (GLAFFMs) and achieves the state-of-the-art SR performance both quantitatively and qualitatively.

## 2 RELATED WORK

The self-similarity has been widely applied to image generation problems. It assumes that similar texture patterns frequently recur within and across scales of the same image. Many classical SISR methods achieve satisfactory SR performance by exploring the self-similarity [5], [6], [7], [11], [28]. The difference between these classical SISR methods in exploring self-similarity is mainly in the range of non-local search space. For example, to reduce the computational complexity of exploring the self-similarity, the search space is usually constrained to some specified local regions [6], [28]. To achieve more accurate reconstruction quality, researchers usually extend the search space of the self-similarity to cross-scale images [5], [7]. In addition, the search space can be further expanded by modeling geometric transformations [11].

Although these classical SISR methods differ in the range of the self-similarity search space, they all follow the same principle of using the self-similarity, which assigns larger weights to non-local textures that are more similar to the query textures. This principle is still used in deep SISR models for exploring the self-similarity information [3], [21], [25], [26], [42]. Specifically, these deep SISR models use cosine similarity to measure the similarity scores between two features and assign higher weights to features with high-similarity. However, as illustrated in Fig. 1, we argue that this principle is not reasonable enough for SISR tasks. This motivates us to explore a learnable similarity scoring method to address this drawback.

In deep learning-based SISR, the non-local attention (NLA) [34] is commonly used to explore the self-similarity.

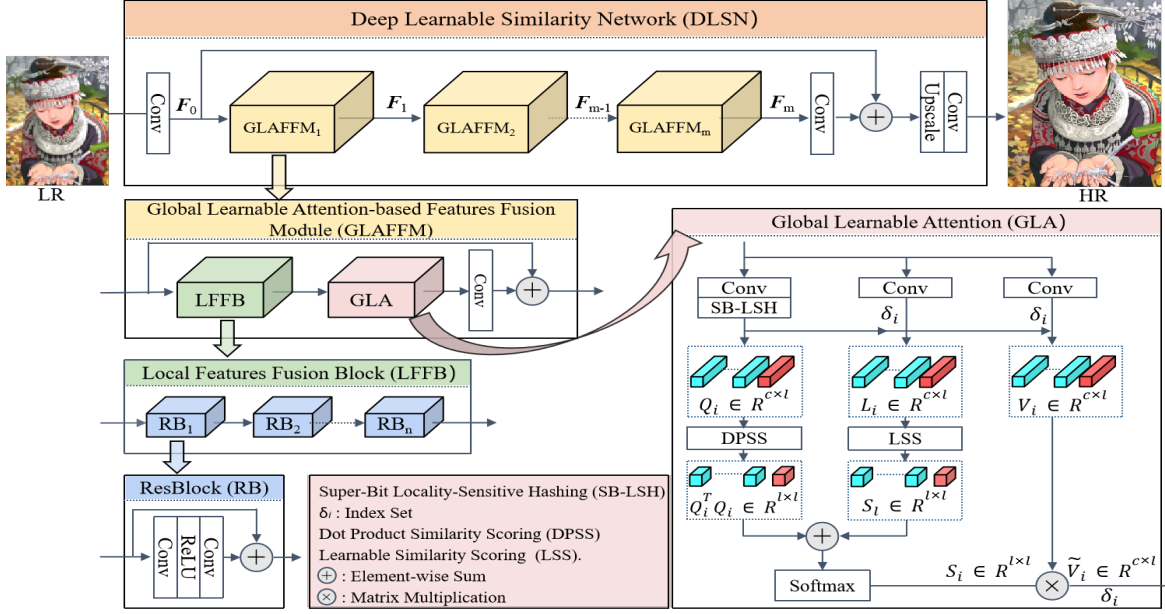


Fig. 2: An illustration of our DLSN. For the convenience of description, we only show the process of  $i$ -th bucket in GLA and the implementation details of the process can be found in Algorithm 1.

However, the computational complexity of the NLA is quadratic to the size of the input image [3], [21], [26], which significantly affects the application of the NLA in deep SISR. Fortunately, there are many approaches to reduce the computational complexity of the NLA by using sparse attention, such as locality sensitive hashing attention [16], [25], routing attention [29], and BigBird [36]. For example, in routing attention [29], the query feature is routed to a limited number of context elements through its cluster assigned by the spherical k-means clustering. Compared with the standard NLA, these sparse attention methods can reduce the complexity significantly by making each feature interact with less but more similar features. Motivated by sparse attention, we propose to adopt the Super-Bit Locality-Sensitive Hashing (SB-LSH) [12] as a preprocessing method of our Global Learnable Attention (GLA). The reason we used SB-LSH to provide sparse attention is that it has two advantages: (1) It only adds negligible extra computation. (2) It is theoretically guaranteed [12] that the SB-LSH can achieve a small hashing variance.

### 3 METHODOLOGY

In this section, we will introduce our Deep Learnable Similarity Network (DLSN) in details. The DLSN consists of a residual backbone with our Global Learnable Attention-based Features Fusion Modules (GLAFFMs). For SISR tasks, there are two kinds of information which are critical for improving the reconstruction results: local adjacency information and learnable non-local self-similarity information. The GLAFFM is designed for fusing these two types of critical information captured by the Local Features Fusion Block (LFFB) and our Global Learnable Attention (GLA), respectively. As discussed in most previous studies, we used the LFFB as a common component to capture the local adjacency information. We start with an overview of

the proposed DLSN and then introduce the details of each component in the GLAFFM.

#### 3.1 Overview of DLSN

As shown in Fig. 2, our DLSN is an end-to-end SR framework which is composed of three parts: low-resolution (LR) features extraction, local and global deep features fusion, and HR image reconstruction. As suggested in [20], [40], only one convolutional layer with trainable parameters  $\alpha$  is used to extract the shallow feature  $F_0$  from the given LR image  $I$ . This procedure can be formally defined as follows

$$F_0 = \Phi(I; \alpha), \quad (3)$$

where  $\Phi(\cdot)$  is the convolution operation in LR features extraction part. Then,  $F_0$  is fed into the local and global deep features fusion part with  $m$  GLAFFMs to obtain refined deep features  $F_m$

$$F_m = \Psi(F_0; \beta), \quad (4)$$

where  $\Psi(\cdot)$  represents the function of our local and global deep feature fusion part with trainable parameters  $\beta$ . Finally, we upscale the obtained deep features  $F_m$  by sub-pixel convolution  $\uparrow$  [30] and then use it to generate a high-resolution image  $\hat{I}$  in the HR image reconstruction part as

$$\hat{I} = \Omega(F_m \uparrow; \gamma), \quad (5)$$

where  $\Omega(\cdot)$  denotes the HR image reconstruction part, which is implemented by a convolutional layer of 3 filters with trainable parameters  $\gamma$  for the final RGB image reconstruction. We can combine the three parts above in our DLSN as

$$\hat{I} = \text{DLSN}(I; (\alpha, \beta, \gamma, \uparrow)), \quad (6)$$

where  $\text{DLSN}(\cdot)$  is the function of our deep learnable similarity network. In addition, to focus on learning high-frequency information and preventing gradients from exploding, we use a long skip connection in the DLSN to directly bypass abundant low-frequency information.

### 3.2 Global Learnable Attention-based Features Fusion Module (GLAFFM)

The structure of GLAFFM is shown in Fig. 2, from which we can see that the GLAFFM serves as a basic module of our DSLN. Specifically, each GLAFFM is also with the residual architecture and consists of a Local Features Fusion Block (LFFB), a Global Learnable Attention (GLA) and a feature refinement convolution layer. The LFFB is responsible for capturing locality inductive bias, while the GLA is exploring global information.

The trainable parameters of GLAFFM are omitted for simplicity and the corresponding function in the  $i$ -th GLAFFM can be defined as

$$\mathbf{F}_i = \Psi_i(\mathbf{F}_{i-1}) = \Psi_i(\Psi_{i-1}(\cdots \Psi_2(\Psi_1(\mathbf{F}_0))), \quad (7)$$

where  $\Psi_i$  represents the function of  $i$ -th GLAFFM.  $\mathbf{F}_{i-1}$  and  $\mathbf{F}_i$  are the input and the output of the  $i$ -th GLAFFM.

#### 3.2.1 Local features fusion block (LFFB)

As discussed in most previous studies [1], [20], we used the LFFB to exploit the locality of the convolution for capturing the local information of nature images. The LFFB is the cornerstone of SR reconstruction, which is formed by stacking  $n$  simplified residual blocks (see Fig. 2 for more details).

#### 3.2.2 Global learnable attention (GLA)

Our GLA can explore global information by summarizing related features from input feature maps. Given the input feature maps  $\mathbf{X} \in R^{h \times w \times c}$ , we reshape it into a 1-D feature  $\mathbf{X}' \in R^{hw \times c}$  for illustration purposes. Then, the attention process of the query feature vector  $\mathbf{x}_i$  can be generally formulated as

$$f(\mathbf{x}_i) = \sum_{j=1}^n \frac{\exp(s(\mathbf{x}_i, \mathbf{x}_j))}{\sum_{k=1}^n \exp(s(\mathbf{x}_i, \mathbf{x}_k))} \phi_v(\mathbf{x}_j), \quad (8)$$

where  $n = hw$ ,  $\mathbf{x}_j$  and  $\mathbf{x}_k$  are the  $j$ -th and  $k$ -th feature vectors on  $\mathbf{X}'$  respectively.  $\phi_v(\cdot)$  is a feature transformation function that generates value vectors.  $s(\cdot, \cdot)$  is used to measure similarity and composes a learnable similarity scoring function  $s_l(\mathbf{x}_i)$  and a fixed dot product similarity scoring function  $s_f(\mathbf{x}_i, \mathbf{x}_j)$

$$s(\mathbf{x}_i, \mathbf{x}_j) = s_l^j(\mathbf{x}_i) + s_f(\mathbf{x}_i, \mathbf{x}_j), \quad (9)$$

where  $s_l^j(\cdot)$  represents the  $j$ -th component in  $s_l(\cdot)$ , and  $s_f(\cdot, \cdot)$  is the standard fixed dot product similarity scoring function, which can be defined as

$$s_f(\mathbf{x}_i, \mathbf{x}_j) = \phi_q(\mathbf{x}_i)^T \phi_k(\mathbf{x}_j), \quad (10)$$

where  $\phi_q(\cdot)$  and  $\phi_k(\cdot)$  are feature transformations which we use to generate query and key vectors. In practice, our GLA shared the parameters in  $\phi_q(\cdot)$  and  $\phi_k(\cdot)$  to reduce the computational cost, and we found that this modification didn't reduce the SR performance.

Existing non-local deep SISR methods [3], [21], [25], [26] assume  $s(\cdot, \cdot) = s_f(\cdot, \cdot)$ , and we have discussed the limitations in Section 1. To overcome the limitations, we proposed a learnable similarity scoring function  $s_l(\cdot)$  to adaptively modify similarity scores. It is worth noting that the similarity scoring function is highly nonlinear and varies

from object to object. Here we used a single hidden layer feedforward neural network (FNN) that has achieved excellent representation ability to revise the fixed dot product similarity scoring. In addition, the modified term learned from the transformed feature  $s_l(\cdot)$  directly through the FNN with a single hidden layer (deeper networks are also possible) has linear computational complexity with respect to the size of the input image. Formally, the learnable similarity scoring function  $s_l(\cdot)$  can be defined as

$$s_l(\mathbf{x}_i) = \mathbf{W}_2 \sigma(\mathbf{W}_1 \phi_l(\mathbf{x}_i) + \mathbf{b}_1) + \mathbf{b}_2, \quad (11)$$

where  $\sigma(\cdot)$  is the ReLU activation and  $\mathbf{x}_i \in R^c$ ,  $\mathbf{W}_1 \in R^{n \times c}$ ,  $\mathbf{b}_1 \in R^n$ ,  $\mathbf{W}_2 \in R^{n \times n}$ ,  $\mathbf{b}_2 \in R^n$ .

### 3.3 Super-Bit Locality-Sensitive Hashing (SB-LSH)

As mentioned in Section 2, the sparse attention has been widely used in deep learning [16], [25], [29], [36] to reduce the computational complexity of the standard non-local attention from quadratic to asymptotic linear by computing the similarity only within each bucket. In this paper, we propose to adopt the SB-LSH [12] to hash global related features into the bucket of the query feature. The SB-LSH provides an estimation of angular similarity with negligible extra computation and shows that the more similar elements are more likely to fall into the same hash bucket. Thus, the SB-LSH can be used as a suitable preprocessing method for our Global Learnable Attention (GLA). Given  $b$  hash buckets, we first project the query feature  $\mathbf{x}_i$  with dimension  $c$  onto an orthonormal basis  $\mathbf{M} \in R^{b \times c}$ :

$$\mathbf{x}'_i = \mathbf{M} \mathbf{x}_i. \quad (12)$$

Then, the assigned hash bucket of  $\mathbf{x}_i$  can be expressed as  $h(\mathbf{x}'_i) = \text{argmax}(\mathbf{x}'_i)$ , where  $\text{argmax}(\cdot)$  finds the index that gives the maximum value from  $\mathbf{x}'_i$ . Finally, global features which are assigned in the same hash bucket  $\lambda_i$  with the query feature  $\mathbf{x}_i$  can be defined as

$$\lambda_i = \{\mathbf{x}_j | h(\mathbf{x}'_i) = h(\mathbf{x}'_j)\}. \quad (13)$$

The SB-LSH is simultaneously performed for all query features with batch matrix multiplication, which only adds negligible extra computation. With the preprocessing method SB-LSH, our GLA can achieve asymptotic linear computational complexity with respect to the size of the input image by computing the non-local attention only within the same hash bucket. Formally, the GLA with the preprocessing method SB-LSH can be derived from Eq. (8) and Eq. (13) as follows

$$f(\mathbf{x}_i) = \sum_{\mathbf{x}_j \in \lambda_i} \frac{\exp(s(\mathbf{x}_i, \mathbf{x}_j))}{\sum_{\mathbf{x}_k \in \lambda_i} \exp(s(\mathbf{x}_i, \mathbf{x}_k))} \phi_v(\mathbf{x}_j), \quad (14)$$

where  $\lambda_i$  contains the features which are assigned in the same hash bucket with the query feature  $\mathbf{x}_i$ . Next, we will introduce some solutions to the problems which arise when using the SB-LSH.

**Uneven bucket size.** In practice, the size of hash buckets tend to be uneven, which makes it difficult to perform parallel computing. To solve the problems, we sort all query features by their bucket number and the sorted permutation is denoted as  $\xi : i \rightarrow \xi(i)$ , where  $\xi(i)$  is the new position

corresponding to the original index  $i$ . Given buckets size  $l$ , the sorted features in the  $k$ -th chunk  $C_k$  can be expressed as

$$C_k = \{\mathbf{x}_{lk+1}, \mathbf{x}_{lk+2}, \dots, \mathbf{x}_{l(k+1)}\}. \quad (15)$$

Finally, the hash bucket  $\lambda_i$  of the query feature  $\mathbf{x}_i$  can be updated as

$$\lambda_i = C_k, \quad (16)$$

where the sorted index  $\xi(i)$  of  $\mathbf{x}_i$  is between  $lk + 1$  and  $l(k + 1)$ . We can now obtain hash buckets of the same size for parallel computing. Some new hash buckets may cross the original bucket boundaries, which can be solved by extending the attention over adjacent buckets. After using adjacent buckets, the search space of non-local features is expanded to  $3l$ .

**Multi-hash SB-LSH.** The hash operation based on SB-LSH has a small probability that similar features are not split into the same bucket. This probability can be reduced by merging the results from multiple rounds of hashing. In the  $r$ -th round of hashing, the result of the query feature  $\mathbf{x}_i$  processed by our GLA (see Eq. (14)) is defined as  $f_r(\mathbf{x}_i)$ . Then, the results of our GLA with multi-hash SB-LSH is regarded as the weighted sum of each hashing attention result. Formally, the multi-hash GLA results  $\hat{\mathbf{x}}_i$  can be obtained by

$$\hat{\mathbf{x}}_i = \sum_r \omega_r f_r(\mathbf{x}_i), \quad (17)$$

where  $\omega_r$  is the weight coefficient of  $r$ -th round hashing. The  $\omega_r$  represents the normalized similarity between the query feature and all features in its assigned  $r$ -th round bucket

$$\omega_r = \frac{\sum_{\mathbf{x}_j \in \lambda_i^r} s(\mathbf{x}_i, \mathbf{x}_j)}{\sum_{\hat{r}=1}^h \sum_{\mathbf{x}_k \in \lambda_i^{\hat{r}}} s(\mathbf{x}_i, \mathbf{x}_k)}, \quad (18)$$

where  $\lambda_i^r$  is a set of global features which are assigned in the same hash bucket with the query feature  $\mathbf{x}_i$  in the  $r$ -th round of hashing.  $h$  is the number of hashing rounds. The effectiveness of the multi-hash SB-LSH will be verified in the experiment section.

More implementation details of our GLA with SB-LSH can be found in Algorithm 1. For illustration, we only show the process of the  $i$ -th bucket in GLA, the remaining buckets are executed in parallel in the same way.

### 3.4 Computational Complexity of Similarity Scoring

Given an input feature  $\mathbf{X} \in R^{h \times w \times c}$ , the standard non-local attention on  $\mathbf{X}$  is  $O((hw)^2c)$  in computational complexity. After hashing the input feature  $\mathbf{X}$  into  $\frac{hw}{l}$  buckets with size  $l$ , the computational complexity of the standard fixed dot product similarity scoring  $s_f(\cdot, \cdot)$  and our learnable similarity scoring function  $s_l(\cdot)$  are  $O(hwlc)$  and  $O(hwlc + hwl^2)$ , respectively. Thus, the computational cost of our GLA in calculating the similarity scores is  $O(2hwlc + hwl^2)$ . It means that our GLA with SB-LSH has asymptotic linear computational complexity with respect to the size of the input image.

---

### Algorithm 1 Global Learnable Attention (GLA) with Super-Bit Locality-Sensitive Hashing (SB-LSH).

---

- 1: **Input:** input features  $\mathbf{X} \in R^{c \times h \times w}$ .
  - 2:  $\mathbf{Q} \leftarrow \text{Conv}(\mathbf{X})$  # convolution with kernel size 3.
  - 3:  $\mathbf{Q} \leftarrow \text{Reshape}(\mathbf{Q})$  # reshape  $\mathbf{Q}$  to  $R^{c \times hw}$ .
  - 4: SB-LSH( $\mathbf{q}_i$ ) #  $\mathbf{q}_i \in R^c$  is the  $i$ -th component of  $\mathbf{Q}$ .
  - 5: randomly initialize a matrix  $\mathbf{H} \in R^{b \times c}$
  - 6:  $\mathbf{M} \leftarrow$  orthogonalize  $\mathbf{H}$  via Gram-Schmidt process
  - 7:  $\mathbf{q}'_i \leftarrow \mathbf{M} \mathbf{q}_i$
  - 8: index  $\leftarrow \text{argmax}(\mathbf{q}'_i)$
  - 9:  $\mathbf{Q}_i \leftarrow \{\}$  #  $\mathbf{Q}_i$  is the hash bucket corresponding to  $\mathbf{q}_i$ .
  
  - 10:  $\delta_i \leftarrow \{\}$  #  $\delta_i$  is the index set corresponding to  $\mathbf{q}_i$ .
  - 11: **for**  $j = 1, \dots, hw$  # this loop can be run in parallel.
  - 12:  $\mathbf{q}'_j \leftarrow \mathbf{M} \mathbf{q}_j$  #  $\mathbf{q}_j$  is the  $j$ -th component of  $\mathbf{Q}$ .
  - 13: **if**  $\text{argmax}(\mathbf{q}'_j) == \text{index}$
  - 14: update  $\mathbf{Q}_i$  by adding  $\mathbf{q}_j$
  - 15: update  $\delta_i$  by adding  $j$
  - 16: **return**  $\mathbf{Q}_i, \delta_i$  #  $\mathbf{Q}_i \in R^{c \times l}$   $\delta_i \in R^l$ .  $l$  is the bucket size.
  - 17:  $\mathbf{L} \leftarrow \text{Conv}(\mathbf{X}), \text{Reshape}(\mathbf{L})$  #  $\mathbf{L} \in R^{c \times hw}$ .
  - 18:  $\mathbf{V} \leftarrow \text{Conv}(\mathbf{X}), \text{Reshape}(\mathbf{V})$  #  $\mathbf{V} \in R^{c \times hw}$ .
  - 19:  $\mathbf{L}_i \leftarrow \mathbf{L}[\delta_i]$  #  $\mathbf{L}_i \in R^{c \times l}$ .
  - 20:  $\mathbf{V}_i \leftarrow \mathbf{V}[\delta_i]$  #  $\mathbf{V}_i \in R^{c \times l}$ .
  - 21: # Dot Product Similarity Scoring (DPSS).
  - 22:  $\mathbf{S}_f \leftarrow \mathbf{Q}_i^T \mathbf{Q}_i$  #  $\mathbf{S}_f \in R^{l \times l}$ .
  - 23: # Learnable Similarity Scoring (LSS).
  - 24:  $\mathbf{S}_l \leftarrow (\mathbf{W}_2 \sigma(\mathbf{W}_1 \mathbf{L}_i + \mathbf{b}_1) + \mathbf{b}_2)$  #  $\mathbf{S}_l \in R^{l \times l}$ .
  - 25:  $\mathbf{S}_i \leftarrow \text{Softmax}(\mathbf{S}_f + \mathbf{S}_l)$  #  $\mathbf{S}_i \in R^{l \times l}$ .
  - 26:  $\tilde{\mathbf{V}}_i \leftarrow \mathbf{V}_i \mathbf{S}_i$  #  $\tilde{\mathbf{V}}_i \in R^{c \times l}$ .
  - 27:  $\mathbf{V}[\delta_i] \leftarrow \tilde{\mathbf{V}}_i$  #  $\mathbf{V} \in R^{c \times hw}$ .
  - 28:  $\mathbf{V} \leftarrow \text{Reshape\_Inverse}(\mathbf{V})$  # reshape  $\mathbf{V}$  to  $R^{c \times h \times w}$ .
  - 29: **Output:**  $\mathbf{V}$
- 

## 4 EXPERIMENTS

### 4.1 Datasets and Evaluation Metrics

Following previous studies [3], [20], [25], [40], we used 800 images from DIV2K [33] as training datasets. Then, we tested our model on five standard SISR benchmarks: Set5 [2], Set14 [37], B100 [23], Urban100 [11], and Manga109 [24]. All the results are evaluated by SSIM [35] and PSNR metrics on the Y channel in YCbCr space.

### 4.2 Implementation Details

Our final DLSN was built on a residual backbone with 10 GLAFFMs. In each GLAFFM, the number of residual blocks in LFFB was set to 4 empirically. All intermediate features have 256 channels, except those in our GLA, which have 64 channels. The last convolution layer in our DLSN has 3 filters to transfer deep features into a 3-channel RGB image. All the convolutional kernel sizes were set to  $3 \times 3$ .

During training, a mini-batch consists of 16 images with patch size  $48 \times 48$  randomly cropped from the training datasets and was augmented by random rotation of 90, 180, and 270 degrees and horizontal flipping. The mean absolute error (MAE) was used as the loss function to train our DLSN. We used ADAM optimizer [15] with  $\beta_1 = 0.9$ ,  $\beta_2 = 0.999$ , and  $\epsilon = 10^{-8}$  to optimize our model. In scale factor  $\times 2$ , the initial learning rate was set to  $10^{-4}$  and

reduced to half every 300 epochs until the training stops at 1500 epochs. When training our models for scale factor  $\times 3$  and  $\times 4$ , we initialized the model parameters with pre-trained  $\times 2$  network and the learning rate  $10^{-4}$  was reduced to half every 50 epochs until the fine-tuning stops at 200 epochs. All our models were implemented by PyTorch and trained on Nvidia 3090 GPUs.

### 4.3 Ablation Study and Analysis

In ablation study, we trained our DLSN on DIV2K [33] for classical SISR with scale factor  $\times 2$  and observed the best PSNR (dB) values on Set14 [37] in  $5 \times 10^4$  iterations.

#### 4.3.1 Impact of LFFB and GLA

The effects of Local Features Fusion Block (LFFB) and Global Learnable Attention (GLA) in our basic unit Global Learnable Attention-based Features Fusion Module (GLAFFM) on SR performance are shown in Table 1.

TABLE 1: Ablation study on GLAFFM (including LFFB and GLA). The best and the second best results are **highlighted** and underlined.

LFFB	$\times$	$\times$	$\checkmark$	$\checkmark$	$\checkmark$
GLA with $s_f(\cdot, \cdot)$	$\checkmark$	$\times$	$\times$	$\checkmark$	$\times$
GLA with $s_f(\cdot, \cdot) + s_l(\cdot)$	$\times$	$\checkmark$	$\times$	$\times$	$\checkmark$
PSNR	33.33	33.49	33.54	<u>33.65</u>	<b>33.77</b>

Note:  $s_f(\cdot, \cdot)$  is the fixed dot product similarity scoring (see Eq.(10)) and  $s_l(\cdot)$  is our learnable similarity scoring (see Eq.(11)).

By comparing the PSNR of the first and second columns in Table 1, we can find that our learnable similarity scoring function  $s_l(\cdot)$  can bring 0.16dB performance improvement on Set14, which is remarkable for Set14 reconstruction. Furthermore, the zoomed in results on Set14 [37], Manga109 [24] and B100 [23] datasets for SR  $\times 4$  are shown in Fig. 3, from which we can see that the network with using our learnable similarity scoring (LSS) can correct some inaccurate textures. Take '78004' (bottom) in B100 [23] as an example, our DLSN with using the LSS successfully recovers the structured architectural textures missed by the network without using the LSS.

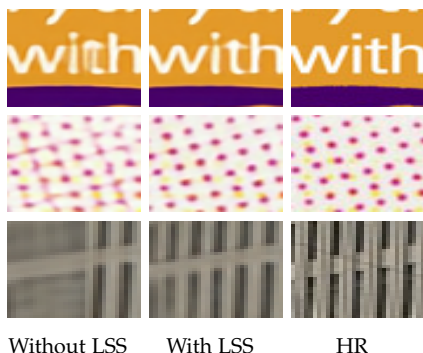


Fig. 3: Comparisons between our DLSN with using our learnable similarity scoring (LSS) and without LSS for  $\times 4$  SR. The textures from top to bottom belong to the 'ppt3', 'WarewareHaOniDearu' and '78004' images from Set14 [37], Manga109 [24] and B100 [23] datasets, respectively.

To observe the mechanism of our LSS for non-local similarity modification, we show the locations of non-local

features (red dots) corresponding to the top 128 weights associated with the query feature (green dot) in the last GLA. As shown in Fig. 4, when the fixed dot product is used for similarity scoring (see the first line in Fig. 4), the associated non-local features are relatively concentrated around the query feature, that is, the fixed dot product tends to give higher weights to non-local features similar to the query feature. On the contrary, after introducing our LSS (see the second line in Fig. 4), an expected change occurs, our DLSN tends to assign higher weights to more informative but low-similarity non-local regions. These results indicate that our LSS can indeed correct the weights of non-local textures, and enable our DLSN to reconstruct more accurate textures by exploring non-local regions with low-similarity but richer textures information.

In Table 1, we can see that locality inductive bias is crucial to SR performance. Without using our LFFB to explore the locality, the SR performance will degrade severely by about 0.3dB. The last column correspond to the GLAFFM used in our DLSN, which can explore local and learnable non-local information simultaneously. We also found that the fixed dot product similarity scoring function  $s_f(\cdot, \cdot)$  is still helpful, and the SR performance can be further improved from 33.65 to 33.77 when composing our learnable similarity scoring function  $s_l(\cdot)$  with  $s_f(\cdot, \cdot)$ .

TABLE 2: Ablation study on the number of hashing rounds.

Train \ Test	Test			
	$h=1$	$h=2$	$h=3$	$h=4$
$h=1$	33.60	33.61	33.61	33.61
$h=2$	33.67	33.69	<u>33.73</u>	33.74
$h=3$	33.68	33.76	<b>33.77</b>	33.77
$h=4$	33.68	33.77	33.78	33.78

#### 4.3.2 Impact of multi-hash SB-LSH and bucket size

**Multi-hash SB-LSH.** As discussed in the Section 3.3, increasing the number of hashing rounds can improve the robustness and effectiveness of our GLA. The number of hashing rounds  $h$  can be set flexibly in the inference stage to find the trade-offs between getting accurate SR performance and reducing computational complexity. The ablation study on hashing rounds  $h$  is shown in Table 2, from which we can see that increasing the number of hashing rounds in training and testing can both improve SR performance. Considering the SR performance and computational complexity, we set  $h$  to be 3 in both training and testing phases in our final DLSN model.

**Bucket Size.** As discussed in the Section 3.3, the bucket size  $l$  determine the number of non-local features that the query feature can explore. The effects of different  $l$  are shown in Fig. 6, from which we can see that the SR performance of our DLSN peaks at  $l = 128$ . When we further enlarging the bucket size, the SR performance starts to degrade. This is mainly because a larger  $l$  reduces the effectiveness of our SB-LSH by merging features across multiple bucket boundaries. Adjusting the bucket size may further improve the reconstruction results, however, it will take a lot of training time to determine the optimal bucket size for each practical dataset. Therefore, we recommend training our DLSN with a relatively appropriate bucket size obtained by our ablation studies. In the extreme case when  $l$  is equal to the size of the



Fig. 4: Non-local location (red dots) comparisons between our DLN with using learnable similarity scoring (LSS) and without LSS for  $\times 4$  SR on Urban100 [23]. The query features are represented by green dots. Please zoom in for best view.

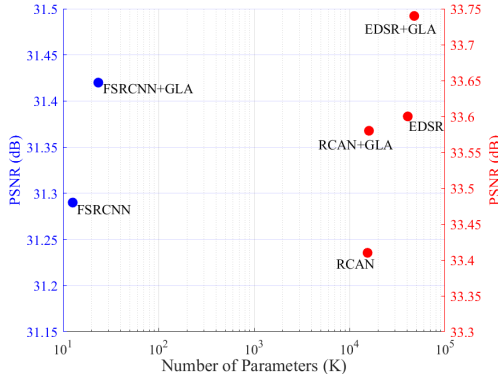


Fig. 5: Parameters vs. performance. Our GLA can improve the SR performance of existing representative SISR models vary in complexity from the simple FSRCNN to the very complex EDSR and RCAN.

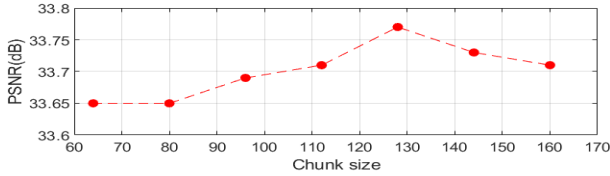


Fig. 6: The PSNR results of different bucket size setting.

input image, our SB-LSH will be ineffective by making our GLA explore all global features.

#### 4.3.3 Versatility of GLA

To analyze the versatility of our GLA, we integrate the GLA into existing representative deep SISR models with the different depths and parameters, such as FSRCNN [4], EDSR [20], and RCAN [40]. From Fig. 5, we observe that our GLA can improve the SR performance of these SISR models significantly. Specifically, our GAL brings 0.13dB, 0.14dB, and 0.17dB improvement for FSRCNN [4], EDSR [20], and RCAN [40], respectively. These results demonstrate that our GLA can be used as an efficient generic block to explore non-local information in deep SISR models.

## 4.4 Efficiency Analysis

**Model Parameters Comparisons.** We compare the model size and SR performance of our DLN with other state-of-the-art deep SISR models including EDSR [20], RDN [41], RCAN [40], DBPN [9], RNAN [39], SAN [3], NLSN [25], IGNN [42]. As shown in Fig. 7, the SR performance of our

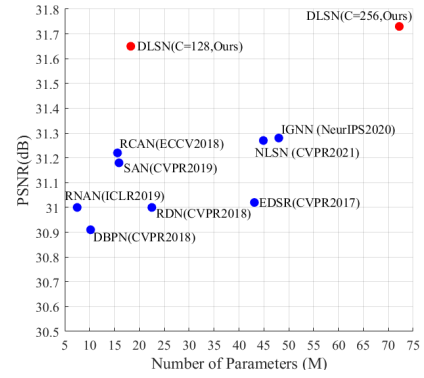


Fig. 7: Model parameters and performance comparisons on Manga109 ( $\times 4$ ).

DLN (C=256) on Manga109 ( $\times 4$ ) is significantly better than other deep SISR models. In addition, the smaller DLN (C=128) which can still achieve remarkable SR performance as compared to the prior state-of-the-art models. Specifically, our DLN (C=128, about 18.27M parameters) brings 0.38dB improvement in SR performance with much lower parameters than NLSN [25] (about 44.9M parameters). It means that the improvement in SR performance for our DLN is not simply the result of having more parameters in the network.

**Inference Time and Memory Comparisons.** To analysis the efficiency of our DLN, we compare the inference time and memory consumption of recently competitive SISR models on the Manga109 dataset with scale factor 4. We also provide a smaller version of our DLN by setting the number of channels C to 128. The inferences of all models are conducted in the same environment with Nvidia 1070Ti GPUs, and the inference time is shown in Fig. 8a. Specifically, by comparing RCAN [40] and NLSN [25], we found that the reconstruction performance of NLSN is 0.05dB higher than that of RCAN at a cost of 114.80 seconds. Furthermore, the reconstruction performance of our DLN (C=128) is not only 0.38dB higher than that of NLSN, but also reduces the inference time by about 18.4 seconds. These results indicate that our DLN is very efficient in improving SR performance, and the similar conclusion can also be obtained by comparing the memory consumption (see Fig. 8b).

## 4.5 Comparisons with State-of-the-art

### 4.5.1 Bicubic-downscale degradation

To verify the effectiveness of the proposed DLN, we compare it with 17 state-of-the-art methods including FSRCNN

TABLE 3: Quantitative results on SISR benchmark datasets. The best and the second best results are **highlighted** and underlined.

Method	Scale	Set5 [2]		Set14 [37]		B100 [23]		Urban100 [11]		Manga109 [24]	
		PSNR	SSIM	PSNR	SSIM	PSNR	SSIM	PSNR	SSIM	PSNR	SSIM
Bicubic	×2	33.66	0.9299	30.24	0.8688	29.56	0.8431	26.88	0.8403	30.80	0.9339
FSRCNN [4]	×2	37.05	0.9560	32.66	0.9090	31.53	0.8920	29.88	0.9020	36.67	0.9710
VDSR [14]	×2	37.53	0.9590	33.05	0.9130	31.90	0.8960	30.77	0.9140	37.22	0.9750
LapSRN [17]	×2	37.52	0.9591	33.08	0.9130	31.08	0.8950	30.41	0.9101	37.27	0.9740
MemNet [32]	×2	37.78	0.9597	33.28	0.9142	32.08	0.8978	31.31	0.9195	37.72	0.9740
SRMDNF [38]	×2	37.79	0.9601	33.32	0.9159	32.05	0.8985	31.33	0.9204	38.07	0.9761
DBPN [9]	×2	38.09	0.9600	33.85	0.9190	32.27	0.9000	32.55	0.9324	38.89	0.9775
EDSR [20]	×2	38.11	0.9602	33.92	0.9195	32.32	0.9013	32.93	0.9351	39.10	0.9773
RDN [41]	×2	38.24	0.9614	34.01	0.9212	32.34	0.9017	32.89	0.9353	39.18	0.9780
RCAN [40]	×2	38.27	0.9614	34.12	0.9216	32.41	0.9027	33.34	0.9384	39.44	0.9786
SAN [3]	×2	38.31	0.9620	34.07	0.9213	32.42	0.9028	33.10	0.9370	39.32	0.9792
OISR [10]	×2	38.21	0.9612	33.94	0.9206	32.36	0.9019	33.03	0.9365	–	–
IGNN [42]	×2	38.24	0.9613	34.12	0.9217	32.41	0.9025	33.23	0.9383	39.35	0.9786
CSNLN [26]	×2	38.28	0.9616	34.07	0.9223	32.40	0.9024	33.25	0.9386	39.37	0.9785
HAN [27]	×2	38.27	0.9614	34.16	0.9217	32.41	0.9027	33.35	0.9385	39.46	0.9785
NLSN [25]	×2	38.34	0.9618	34.08	0.9231	32.43	0.9027	33.42	0.9394	39.59	0.9789
DRLN [1]	×2	38.27	0.9616	34.28	0.9231	32.44	0.9028	33.37	0.9390	39.58	0.9786
SwinIR [19]	×2	38.35	0.9620	34.14	0.9227	32.44	0.9030	33.40	0.9393	39.60	0.9792
DLSN(ours)	×2	<u>38.43</u>	<u>0.9622</u>	<u>34.44</u>	<u>0.9245</u>	<u>32.46</u>	<u>0.9036</u>	<u>33.70</u>	<u>0.9415</u>	<u>39.70</u>	<u>0.9793</u>
DLSN+(ours)	×2	<b>38.49</b>	<b>0.9624</b>	<b>34.51</b>	<b>0.9251</b>	<b>32.53</b>	<b>0.9042</b>	<b>33.98</b>	<b>0.9432</b>	<b>39.89</b>	<b>0.9797</b>
Bicubic	×3	30.39	0.8682	27.55	0.7742	27.21	0.7385	24.46	0.7349	26.95	0.8556
FSRCNN [4]	×3	33.18	0.9140	29.37	0.8240	28.53	0.7910	26.43	0.8080	31.10	0.9210
VDSR [14]	×3	33.67	0.9210	29.78	0.8320	28.83	0.7990	27.14	0.8290	32.01	0.9340
LapSRN [17]	×3	33.82	0.9227	29.87	0.8320	28.82	0.7980	27.07	0.8280	32.21	0.9350
MemNet [32]	×3	34.09	0.9248	30.00	0.8350	28.96	0.8001	27.56	0.8376	32.51	0.9369
SRMDNF [38]	×3	34.12	0.9254	30.04	0.8382	28.97	0.8025	27.57	0.8398	33.00	0.9403
EDSR [20]	×3	34.65	0.9280	30.52	0.8462	29.25	0.8093	28.80	0.8653	34.17	0.9476
RDN [41]	×3	34.71	0.9296	30.57	0.8468	29.26	0.8093	28.80	0.8653	34.13	0.9484
RCAN [40]	×3	34.74	0.9299	30.65	0.8482	29.32	0.8111	29.09	0.8702	34.44	0.9499
SAN [3]	×3	34.75	0.9300	30.59	0.8476	29.33	0.8112	28.93	0.8671	34.30	0.9494
OISR [10]	×3	34.72	0.9297	30.57	0.8470	29.29	0.8103	28.95	0.8680	–	–
IGNN [42]	×3	34.72	0.9298	30.66	0.8484	29.31	0.8105	29.03	0.8696	34.39	0.9496
CSNLN [26]	×3	34.74	0.9300	30.66	0.8482	29.33	0.8105	29.13	0.8712	34.45	0.9502
HAN [27]	×3	34.75	0.9299	30.67	0.8483	29.32	0.8110	29.10	0.8705	34.48	0.9500
NLSN [25]	×3	34.85	0.9306	30.70	0.8485	29.34	0.8117	29.25	0.8726	34.57	0.9508
DRLN [1]	×3	34.78	0.9303	30.73	0.8488	29.36	0.8117	29.21	0.8722	34.71	0.9509
SwinIR [19]	×3	34.89	0.9312	30.77	0.8503	29.37	0.8124	29.29	0.8744	34.74	0.9518
DLSN(ours)	×3	<u>34.92</u>	<u>0.9308</u>	<u>30.80</u>	<u>0.8509</u>	<u>29.41</u>	<u>0.8136</u>	<u>29.54</u>	<u>0.8775</u>	<u>34.90</u>	<u>0.9522</u>
DLSN+(ours)	×3	<b>35.02</b>	<b>0.9315</b>	<b>30.90</b>	<b>0.8521</b>	<b>29.47</b>	<b>0.8145</b>	<b>29.77</b>	<b>0.8805</b>	<b>35.20</b>	<b>0.9535</b>
Bicubic	×4	28.42	0.8104	26.00	0.7027	25.96	0.6675	23.14	0.6577	24.89	0.7866
FSRCNN [4]	×4	30.72	0.8660	27.61	0.7550	26.98	0.7150	24.62	0.7280	27.90	0.8610
VDSR [14]	×4	31.35	0.8830	28.02	0.7680	27.29	0.7026	25.18	0.7540	28.83	0.8870
LapSRN [17]	×4	31.54	0.8850	28.19	0.7720	27.32	0.7270	25.21	0.7560	29.09	0.8900
MemNet [32]	×4	31.74	0.8893	28.26	0.7723	27.40	0.7281	25.50	0.7630	29.42	0.8942
SRMDNF [38]	×4	31.96	0.8925	28.35	0.7787	27.49	0.7337	25.68	0.7731	30.09	0.9024
DBPN [9]	×4	32.47	0.8980	28.82	0.7860	27.72	0.7400	26.38	0.7946	30.91	0.9137
EDSR [20]	×4	32.46	0.8968	28.80	0.7876	27.71	0.7420	26.64	0.8033	31.02	0.9148
RDN [41]	×4	32.47	0.8990	28.81	0.7871	27.72	0.7419	26.61	0.8028	31.00	0.9151
RCAN [40]	×4	32.63	0.9002	28.87	0.7889	27.77	0.7436	26.82	0.8087	31.22	0.9173
SAN [3]	×4	32.64	0.9003	28.92	0.7888	27.78	0.7436	26.79	0.8068	31.18	0.9169
OISR [10]	×4	32.53	0.8992	28.86	0.7878	27.75	0.7428	26.79	0.8068	–	–
IGNN [42]	×4	32.57	0.8998	28.85	0.7891	27.77	0.7434	26.84	0.8090	31.28	0.9182
CSNLN [26]	×4	32.68	0.9004	28.95	0.7888	27.80	0.7439	27.22	0.8168	31.43	0.9201
HAN [27]	×4	32.64	0.9002	28.90	0.7890	27.80	0.7442	26.85	0.8094	31.42	0.9177
NLSN [25]	×4	32.59	0.9000	28.87	0.7891	27.78	0.7444	26.96	0.8109	31.27	0.9184
DRLN [1]	×4	32.63	0.9002	28.94	0.7900	27.83	0.7444	26.98	0.8119	31.54	0.9196
SwinIR [19]	×4	32.72	0.9021	28.94	0.7914	27.83	0.7459	27.07	0.8164	31.67	0.9226
DLSN(ours)	×4	<u>32.81</u>	<u>0.9012</u>	<u>29.02</u>	<u>0.7914</u>	<u>27.85</u>	<u>0.7468</u>	<u>27.26</u>	<u>0.8191</u>	<u>31.73</u>	<u>0.9224</u>
DLSN+(ours)	×4	<b>32.95</b>	<b>0.9026</b>	<b>29.14</b>	<b>0.7938</b>	<b>27.92</b>	<b>0.7483</b>	<b>27.49</b>	<b>0.8235</b>	<b>32.10</b>	<b>0.9252</b>

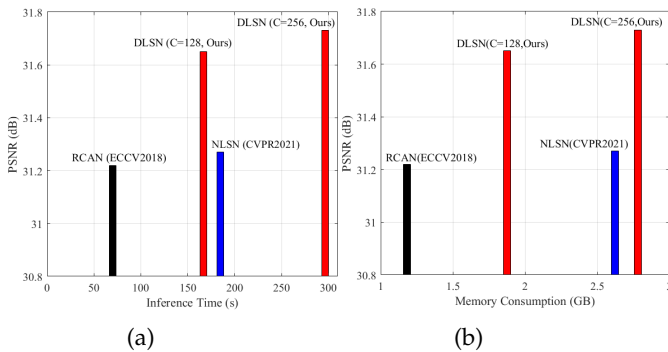


Fig. 8: The PSNR results in (a) and (b) are test on Manga109 with scale factor 4. (a) Inference time comparisons on Manga109 (×4). (b) Memory consumption comparisons on an input image with size  $128 \times 128$ .

[4], VDSR [14], LapSRN [17], EDSR [20], MemNet [32], SRMDNF [38], DBPN [9], RDN [41], RCAN [40], SAN [3], OISR [10], IGNN [42], CSNLN [26], HAN [27], NLSN [25], DRLN [1], and SwinIR [19]. DLSN+ is the self ensemble results of our DLSN.

**Quantitative Evaluations.** The quantitative comparisons with different scale factors are shown in Table 3, where we report the quantitative comparisons between our DLSN and 17 state-of-the-art deep SISR methods on five benchmark datasets for scale factor  $\times 2$ ,  $\times 3$  and  $\times 4$ . From Table 3, we can see that our DLSN outperforms other state-of-the-art deep SISR models by a large margin on almost all benchmarks and scale factors. For example, compared with impressive NLSN [25] in scale factor  $\times 3$ , our DLSN has 0.07dB, 0.10dB, 0.07dB, 0.29dB and 0.33dB performance improvement on Set5, Set14, B100, Urban100 and Manga109



TABLE 4: Quantitative results on benchmark datasets with blur-downscale degradation. The best and the second best results are **highlighted** and underlined.

Method	Scale	Set5 [2]		Set14 [37]		B100 [23]		Urban100 [11]		Manga109 [24]	
		PSNR	SSIM	PSNR	SSIM	PSNR	SSIM	PSNR	SSIM	PSNR	SSIM
Bicubic	$\times 3$	28.78	0.8308	26.38	0.7271	26.33	0.6918	23.52	0.6862	25.46	0.8149
FSRCNN [4]	$\times 3$	32.33	0.9020	28.91	0.8122	28.17	0.7791	25.71	0.7842	29.37	0.8985
VDSR [14]	$\times 3$	33.25	0.9150	29.46	0.8244	28.57	0.7893	26.61	0.8136	31.06	0.9234
SRMDNF [38]	$\times 3$	34.01	0.9242	30.11	0.8364	28.98	0.8009	27.50	0.8370	32.97	0.9391
RDN [41]	$\times 3$	34.58	0.9280	30.53	0.8447	29.23	0.8079	28.46	0.8582	33.97	0.9465
EDSR [20]	$\times 3$	34.64	0.9282	30.54	0.8451	29.27	0.8094	28.64	0.8618	34.13	0.9477
RCAN [40]	$\times 3$	34.70	0.9288	30.63	0.8462	29.32	0.8093	28.81	0.8647	34.38	0.9483
SAN [3]	$\times 3$	34.75	0.9290	30.68	0.8466	29.33	0.8101	28.83	0.8646	34.46	0.9487
HAN [27]	$\times 3$	34.76	0.9294	30.70	0.8475	29.34	0.8106	28.99	0.8676	34.56	0.9494
DLSN(Ours)	$\times 3$	<b>34.93</b>	<b>0.9300</b>	<b>30.80</b>	<b>0.8492</b>	<b>29.42</b>	<b>0.8126</b>	<b>29.38</b>	<b>0.8740</b>	<b>34.98</b>	<b>0.9515</b>
DLSN+(Ours)	$\times 3$	<b>35.02</b>	<b>0.9307</b>	<b>30.92</b>	<b>0.8506</b>	<b>29.48</b>	<b>0.8136</b>	<b>29.62</b>	<b>0.8772</b>	<b>35.29</b>	<b>0.9529</b>



Fig. 9: Visual comparisons for  $\times 3$  SISR with blur-downscale degradation on the Set14. The best result is **highlighted**.

datasets, respectively. The proposed DLSN can achieve significant improvements on challenging datasets Urban100 and Manga109, which contain extensive repeated textures.

On Urban100 ( $\times 2$ ) dataset, which is designed for analyzing the self-similarity, we can see that recent deep SISR models have made very limited improvements on this dataset. For example, even though NLSN [25] integrates impressive sparse non-local attention in deep SISR models for exploring the self-similarity, PSNR only increases by 0.08dB from RCAN (ECCV2018) [40] to NLSN (CVPR2021) [25]. In contrast, our DLSN achieves a significant improvement on this dataset: we bring 0.36dB improvement in PSNR compared to RCAN [40]. The improvement is consistent with our motivation to design the GLA, which aims to capture the self-similarity information in LR images efficiently.

**Qualitative Evaluations.** Visual comparisons on Urban100 and Manga109 with scale factor  $\times 4$  are shown in Fig. 10 and Fig. 11, from both of which we can see that the proposed DLSN can restore the severely damaged textures when the corresponding non-local information can be found in LR images. On the contrary, deep SISR models without non-local attention cannot reconstruct severely damaged textures accurately. For example, by comparing the reconstruction results of image ‘img\_092’ in Fig. 10, we observe that the generated results of our DLSN is very close to the HR, but the other very competitive deep SISR models without non-local attention such as EDSR [20], RCAN [40] are not suitable for recovering such severely damaged regions. Moreover, compared with the other non-local deep SISR methods such as SAN [3] and NLSN [25], our DLSN still maintains better reconstruction quality with more accurate textures. These comparison shows that our DLSN is more efficient in repairing severely damaged regions by exploring

TABLE 5: Quantitative results on Set14 [37] ( $\times 3$ ) with noise-downscale degradation in  $5 \times 10^4$  iterations. The best and the second best results are **highlighted** and underlined.

Noise level	FSRCNN [4]	EDSR [20]	RCAN [40]	DLSN(Ours)
	PSNR/SSIM	PSNR/SSIM	PSNR/SSIM	PSNR/SSIM
10	27.26/0.7396	<b>28.77/0.7892</b>	28.76/0.7883	<b>28.91/0.7903</b>
15	26.58/0.7123	<b>28.11/0.7653</b>	28.06/0.7622	<b>28.20/0.7671</b>
20	25.99/0.6875	<b>27.52/0.7442</b>	27.48/0.7415	<b>27.62/0.7463</b>
25	25.51/0.6674	<b>26.99/0.7241</b>	26.99/0.7232	<b>27.09/0.7279</b>

the self-similarity information with the proposed non-local method GLA.

The visual results demonstrate that our DLSN not only outperforms in quantitative metrics, but also perceptually better than the other deep SISR models by a large margin. In addition, more visual comparisons between our DLSN and some significant SISR methods including DRLN [1] and SwinIR [19] can be found in our supplementary file.

#### 4.5.2 Blur-downscale degradation

Our DLSN is verified on blur-downscale degradation SISR tasks with scale factor  $\times 3$  and the gaussian standard deviation is set to 1.6 as discussed in SRMDNF [38] and RCAN [40]. The quantitative results of our DLSN are compared with the other 8 state-of-the-art methods: FSRCNN [4], VDSR [14], EDSR [20], SRMDNF [38], RDN [41], RCAN [40], SAN [3] and HAN [27].

**Quantitative Evaluations.** The quantitative comparisons of blur-downscale degradation with scale factor  $\times 3$  are shown in Table 4. From Table 4, we can see that our DLSN outperforms the very deep SISR model HAN [27], which has a well-engineered structure with the holistic attention. Specifically, compared with HAN, our DLSN has 0.17dB, 0.10dB, 0.08dB, 0.39dB and 0.42dB improvement on Set5, Set14, B100, Urban100 and Manga109 datasets, respectively. These results mean that our DLSN can still achieve very impressive SR performance when solving SISR tasks with blur-downscale degradation.

**Qualitative Evaluations.** Visual comparisons on Set14 datasets with blur-downscale degradation are shown in Fig. 9, from which we can see that our DLSN generates the most visual pleasing textures with accurate image details. From Fig. 9, we can also find that EDSR [20] cannot restore textures which are severely damaged by blur-downscale degradation, even though the selected region has informative repeated textures in the tablecloth of the input LR image. These visual results show that our DLSN is indeed effective when dealing with blur-downscale SISR tasks.

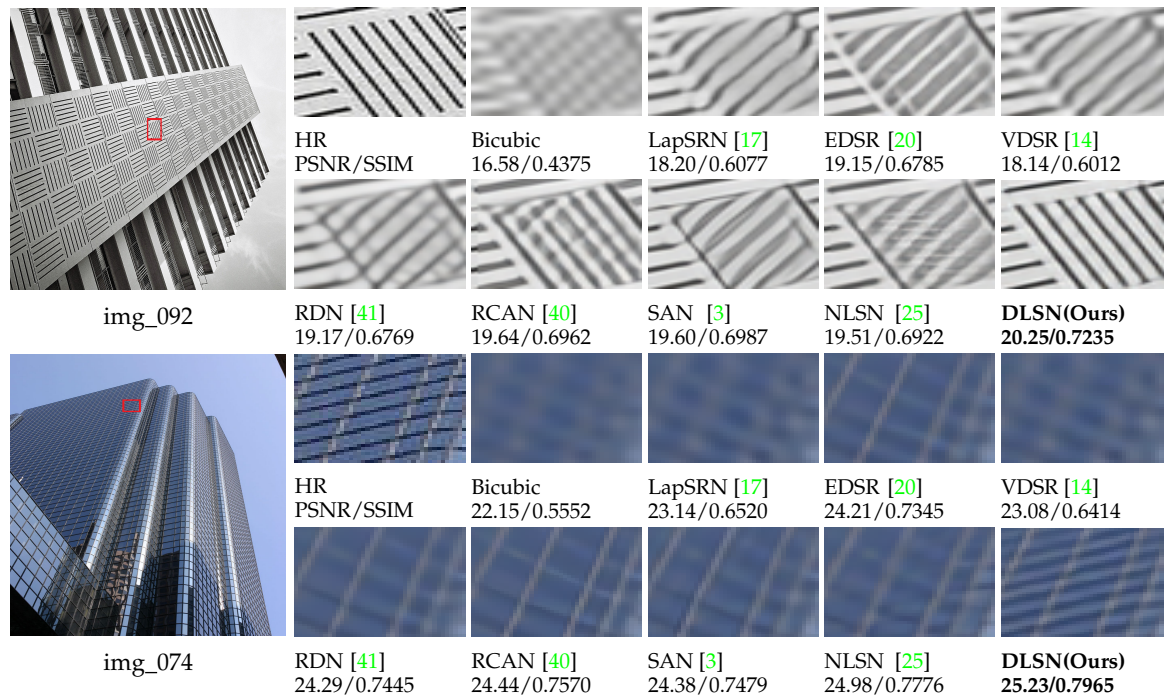


Fig. 10: Visual comparisons on Urban100 [11] with scale factor 4.

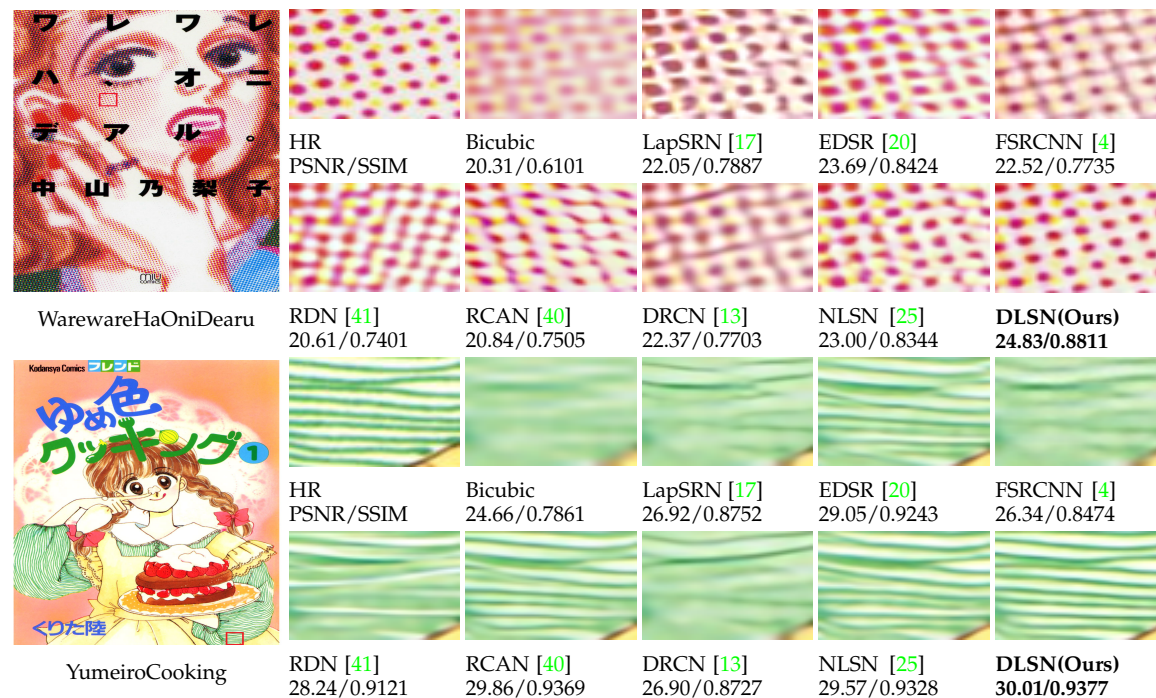


Fig. 11: Visual comparisons on Manga109 [24] with scale factor 4.

#### 4.5.3 Noisy-downscale degradation

To verify the robustness of our DLSN in handling noisy-downscale degradation, we reimplemented some state-of-the-art deep SISR models under the same training datasets and compared them with our DLSN. Table 5 shows the SR performance of these state-of-the-art SISR models at noise levels of 10, 15, 20, and 25, respectively. From Table 5, we can see that our DLSN outperforms other state-of-the-art SISR models at all noise levels, which indicates that our DLSN is robust in handling SISR tasks with different noise levels.

#### 4.5.4 Reference-based SISR

We also provided the comparisons with some significant reference-based SISR methods, including MASA [22]. Compared with reference-based SISR methods, our DLSN can still achieve competitive reconstruction performance without using the reference images. Please refer to the supplementary file for detailed comparisons.

#### 4.5.5 Real-world images super-resolution

In this section, we provided the performance comparisons on real-world historic images with JPEG compression arti-

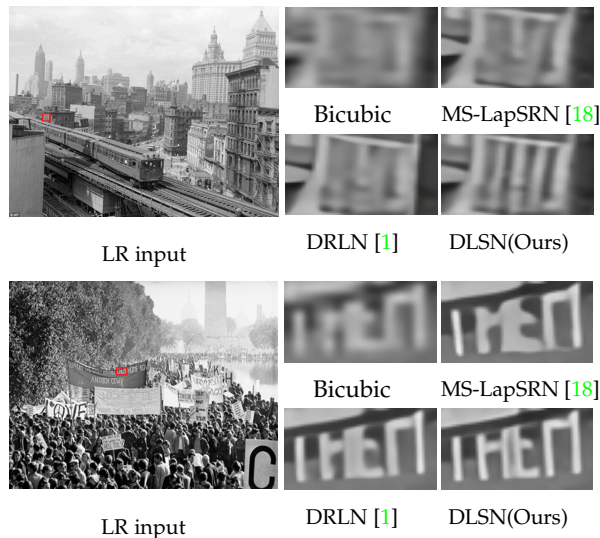


Fig. 12: Visual comparisons on real-world images for scale factor 4. On the bottom LR input, Our DLSN recovers the letter “H” appropriately while DRLN and MS-LapSRN incorrectly connect the stroke with the letter “E”.

facts, as discussed in MS-LapSRN [18] and DRLN [1]. From Fig. 12, we can see that on the top LR input, our DLSN reconstructs more accurate structured architectural textures than the competitive MS-LapSRN and DRLN. Furthermore, compared with the results of Bicubic, we can observe that when the input letters are seriously damaged, our DLSN can still generate sharp and clear edges of the letters.

#### 4.6 Limitations

Although our DLSN can reconstruct visually pleasing results, it struggles to “hallucinate” fine details if the input textures are completely destroyed. This is a common limitation shared by classic deep SISR methods including RCAN [40], NLSN [25] and DRLN [1]. For example, as shown in Fig. 13, all the classic deep SISR methods failed to repair the completely destroyed structured architectural region. The main reason for the limitation is that the completely destroyed input region lacks the basic texture patterns for the reconstruction.

## 5 CONCLUSION

In this paper, we provided new insights into the self-similarity in SISR tasks and found some critical limitations presenting in the existing deep self-similarity-based methods. To overcome these drawbacks, we design a flexible global learnable attention-based features fusion module (GLAFFM) that can make our deep learnable similarity network (DLSN) focus on more valuable non-local textures to repair severely damaged regions. Furthermore, with the super-bit locality-sensitive hashing (SB-LSH), our GLAFFM can achieve asymptotic linear computational complexity with respect to the image size when computing non-local attention. In addition, extensive experiments demonstrate that our GLA can handle SISR tasks with different degradation types (e.g. blur and noise), and can be integrated as an efficient general building block in deep SISR models.

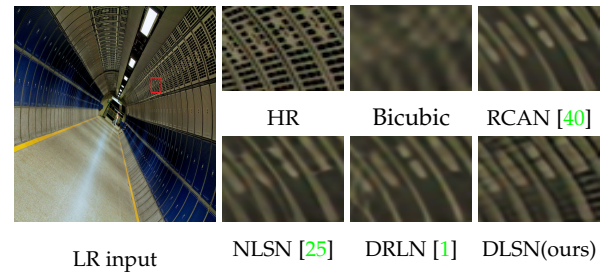
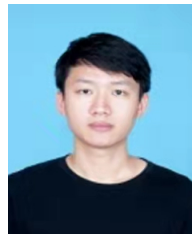


Fig. 13: Limitation. A failure case for repairing completely destroyed regions. Our method is not able to hallucinate details if the input regions lack the basic texture patterns for the reconstruction.

## REFERENCES

- [1] S. Anwar and N. Barnes, “Densely residual laplacian super-resolution,” *IEEE Transactions on Pattern Analysis & Machine Intelligence*, vol. 44, no. 03, pp. 1192–1204, 2022. 4, 8, 9, 11
- [2] M. Bevilacqua, A. Roumy, C. Guillemot, and M. L. Alberi-Morel, “Low-complexity single-image super-resolution based on nonnegative neighbor embedding,” 2012. 5, 8, 9
- [3] T. Dai, J. Cai, Y. Zhang, S.-T. Xia, and L. Zhang, “Second-order attention network for single image super-resolution,” in *Proceedings of the IEEE/CVF Conference on Computer Vision and Pattern Recognition*, 2019, pp. 11 065–11 074. 1, 2, 3, 4, 5, 7, 8, 9, 10
- [4] C. Dong, C. C. Loy, and X. Tang, “Accelerating the super-resolution convolutional neural network,” in *European conference on computer vision*. Springer, 2016, pp. 391–407. 1, 2, 7, 8, 9, 10
- [5] M. Ebrahimi and E. R. Vrscay, “Solving the inverse problem of image zooming using “self-examples”,” in *International Conference Image Analysis and Recognition*. Springer, 2007, pp. 117–130. 1, 2
- [6] G. Freedman and R. Fattal, “Image and video upscaling from local self-examples,” *ACM Transactions on Graphics (TOG)*, vol. 30, no. 2, pp. 1–11, 2011. 2
- [7] D. Glasner, S. Bagon, and M. Irani, “Super-resolution from a single image,” in *2009 IEEE 12th international conference on computer vision*. IEEE, 2009, pp. 349–356. 1, 2
- [8] M. Haris, G. Shakhnarovich, and N. Ukita, “Task-driven super resolution: Object detection in low-resolution images,” in *International Conference on Neural Information Processing*. Springer, 2021, pp. 387–395. 1
- [9] —, “Deep back-projection networks for super-resolution,” in *Proceedings of the IEEE conference on computer vision and pattern recognition*, 2018, pp. 1664–1673. 7, 8
- [10] X. He, Z. Mo, P. Wang, Y. Liu, M. Yang, and J. Cheng, “Ode-inspired network design for single image super-resolution,” in *Proceedings of the IEEE/CVF Conference on Computer Vision and Pattern Recognition*, 2019, pp. 1732–1741. 8
- [11] J.-B. Huang, A. Singh, and N. Ahuja, “Single image super-resolution from transformed self-exemplars,” in *Proceedings of the IEEE conference on computer vision and pattern recognition*, 2015, pp. 5197–5206. 1, 2, 5, 8, 9, 10
- [12] J. Ji, J. Li, S. Yan, B. Zhang, and Q. Tian, “Super-bit locality-sensitive hashing,” *Advances in neural information processing systems*, vol. 25, 2012. 2, 3, 4
- [13] J. Kim, J. Kwon Lee, and K. Mu Lee, “Deeply-recursive convolutional network for image super-resolution,” in *IEEE Conference on Computer Vision and Pattern Recognition*, Las Vegas, Nevada, June 2016, pp. 1637–1645. 10
- [14] J. Kim, J. K. Lee, and K. M. Lee, “Accurate image super-resolution using very deep convolutional networks,” in *Proceedings of the IEEE conference on computer vision and pattern recognition*, 2016, pp. 1646–1654. 8, 9, 10
- [15] A. Kinga, “A method for stochastic optimization,” *Anon. International Conference on Learning Representations*. SanDeGo: ICLR, 2015. 5
- [16] N. Kitaev, L. Kaiser, and A. Levskaya, “Reformer: The efficient transformer,” in *International Conference on Learning Representations*, 2019. 3, 4
- [17] W.-S. Lai, J.-B. Huang, N. Ahuja, and M.-H. Yang, “Deep laplacian pyramid networks for fast and accurate super-resolution,” in

- Proceedings of the IEEE conference on computer vision and pattern recognition*, 2017, pp. 624–632. 8, 10
- [18] —, “Fast and accurate image super-resolution with deep laplacian pyramid networks,” *IEEE transactions on pattern analysis and machine intelligence*, vol. 41, no. 11, pp. 2599–2613, 2018. 11
- [19] J. Liang, J. Cao, G. Sun, K. Zhang, L. Van Gool, and R. Timofte, “Swinir: Image restoration using swin transformer,” in *Proceedings of the IEEE/CVF International Conference on Computer Vision*, 2021, pp. 1833–1844. 8, 9
- [20] B. Lim, S. Son, H. Kim, S. Nah, and K. Mu Lee, “Enhanced deep residual networks for single image super-resolution,” in *Proceedings of the IEEE conference on computer vision and pattern recognition workshops*, 2017, pp. 136–144. 1, 2, 3, 4, 5, 7, 8, 9, 10
- [21] D. Liu, B. Wen, Y. Fan, C. C. Loy, and T. S. Huang, “Non-local recurrent network for image restoration,” *Advances in Neural Information Processing Systems*, vol. 2018, pp. 1673–1682, 2018. 1, 2, 3, 4
- [22] L. Lu, W. Li, X. Tao, J. Lu, and J. Jia, “Masa-sr: Matching acceleration and spatial adaptation for reference-based image super-resolution,” in *Proceedings of the IEEE/CVF Conference on Computer Vision and Pattern Recognition*, 2021, pp. 6368–6377. 10
- [23] D. Martin, C. Fowlkes, D. Tal, and J. Malik, “A database of human segmented natural images and its application to evaluating segmentation algorithms and measuring ecological statistics,” in *Proceedings Eighth IEEE International Conference on Computer Vision. ICCV 2001*, vol. 2. IEEE, 2001, pp. 416–423. 5, 6, 7, 8, 9
- [24] Y. Matsui, K. Ito, Y. Aramaki, A. Fujimoto, T. Ogawa, T. Yamasaki, and K. Aizawa, “Sketch-based manga retrieval using manga109 dataset,” *Multimedia Tools and Applications*, vol. 76, no. 20, pp. 21 811–21 838, 2017. 5, 6, 8, 9, 10
- [25] Y. Mei, Y. Fan, and Y. Zhou, “Image super-resolution with non-local sparse attention,” in *Proceedings of the IEEE/CVF Conference on Computer Vision and Pattern Recognition*, 2021, pp. 3517–3526. 1, 2, 3, 4, 5, 7, 8, 9, 10, 11
- [26] Y. Mei, Y. Fan, Y. Zhou, L. Huang, T. S. Huang, and H. Shi, “Image super-resolution with cross-scale non-local attention and exhaustive self-exemplars mining,” in *Proceedings of the IEEE/CVF Conference on Computer Vision and Pattern Recognition*, 2020, pp. 5690–5699. 1, 2, 3, 4, 8
- [27] B. Niu, W. Wen, W. Ren, X. Zhang, L. Yang, S. Wang, K. Zhang, X. Cao, and H. Shen, “Single image super-resolution via a holistic attention network,” in *European conference on computer vision*. Springer, 2020, pp. 191–207. 8, 9
- [28] M. Protter, M. Elad, H. Takeda, and P. Milanfar, “Generalizing the nonlocal-means to super-resolution reconstruction,” *IEEE Transactions on image processing*, vol. 18, no. 1, pp. 36–51, 2008. 2
- [29] A. Roy, M. Saffar, A. Vaswani, and D. Grangier, “Efficient content-based sparse attention with routing transformers,” *Transactions of the Association for Computational Linguistics*, vol. 9, pp. 53–68, 2021. 3, 4
- [30] W. Shi, J. Caballero, F. Huszár, J. Totz, A. P. Aitken, R. Bishop, D. Rueckert, and Z. Wang, “Real-time single image and video super-resolution using an efficient sub-pixel convolutional neural network,” in *IEEE Conference on Computer Vision and Pattern Recognition*, Las Vegas, America, June 2016, pp. 1874–1883. 3
- [31] Y. Sui, O. Afacan, C. Jaimes, A. Gholipour, and S. K. Warfield, “Scan-specific generative neural network for mri super-resolution reconstruction,” *IEEE Transactions on Medical Imaging*, 2022. 1
- [32] Y. Tai, J. Yang, X. Liu, and C. Xu, “Memnet: A persistent memory network for image restoration,” in *IEEE International Conference on Computer Vision*, Venice, Italy, October 2017, pp. 4539–4547. 8
- [33] R. Timofte, E. Agustsson, L. Van Gool, M.-H. Yang, and L. Zhang, “Ntire 2017 challenge on single image super-resolution: Methods and results,” in *Proceedings of the IEEE conference on computer vision and pattern recognition workshops*, 2017, pp. 114–125. 5, 6
- [34] X. Wang, R. Girshick, A. Gupta, and K. He, “Non-local neural networks,” in *Proceedings of the IEEE conference on computer vision and pattern recognition*, 2018, pp. 7794–7803. 1, 2
- [35] Z. Wang, A. C. Bovik, H. R. Sheikh, and E. P. Simoncelli, “Image quality assessment: from error visibility to structural similarity,” *IEEE transactions on image processing*, vol. 13, no. 4, pp. 600–612, 2004. 5
- [36] M. Zaheer, G. Guruganesh, K. A. Dubey, J. Ainslie, C. Alberti, S. Ontanon, P. Pham, A. Ravula, Q. Wang, L. Yang *et al.*, “Big bird: Transformers for longer sequences,” *Advances in Neural Information Processing Systems*, vol. 33, pp. 17 283–17 297, 2020. 3, 4
- [37] R. Zeyde, M. Elad, and M. Protter, “On single image scale-up using sparse-representations,” in *International conference on curves and surfaces*. Springer, 2010, pp. 711–730. 5, 6, 8, 9
- [38] K. Zhang, W. Zuo, and L. Zhang, “Learning a single convolutional super-resolution network for multiple degradations,” in *Proceedings of the IEEE Conference on Computer Vision and Pattern Recognition*, 2018, pp. 3262–3271. 8, 9
- [39] Y. Zhang, K. Li, B. Zhong, and Y. Fu, “Residual non-local attention networks for image restoration,” in *International Conference on Learning Representations*, 2019. 7
- [40] Y. Zhang, K. Li, K. Li, L. Wang, B. Zhong, and Y. Fu, “Image super-resolution using very deep residual channel attention networks,” in *European Conference on Computer Vision (ECCV)*, Munich, Germany, September 2018, pp. 286–301. 2, 3, 5, 7, 8, 9, 10, 11
- [41] Y. Zhang, Y. Tian, Y. Kong, B. Zhong, and Y. Fu, “Residual dense network for image super-resolution,” in *IEEE Conference on Computer Vision and Pattern Recognition*, Salt Lake City, Utah, June 2018, pp. 2472–2481. 2, 7, 8, 9, 10
- [42] S. Zhou, J. Zhang, W. Zuo, and C. C. Loy, “Cross-scale internal graph neural network for image super-resolution,” *Advances in neural information processing systems*, vol. 33, pp. 3499–3509, 2020. 2, 7, 8
- [43] M. Zontak and M. Irani, “Internal statistics of a single natural image,” in *CVPR 2011*. IEEE, 2011, pp. 977–984. 1



**Jian-Nan Su** received the B.S. and M.S. degree in computer science and engineering from Fuzhou University, Fuzhou, China, in 2015 and 2018. He is currently pursuing the Ph.D. degree with the College of Computer and Data Science, Fuzhou University, Fuzhou, China. His current research interests include image processing and machine learning.



**Min Gan** received the B.S. degree in computer science and engineering from the Hubei University of Technology, Wuhan, China, in 2004, and the Ph.D. degree in control science and engineering from Central South University, Changsha, China, in 2010. He is currently a Professor with the College of Computer and Data Science, Fuzhou University, Fuzhou, China. His current research interests include statistical learning, system identification, and nonlinear time-series analysis, image processing.



**Guang-Yong Chen** received the B.S. degree in mathematics from Xidian University, Xi’an, China, in 2012, and the M.S. degree in mathematics from the University of Science and Technology of China, Hefei, China, in 2014, and the Ph.D. degree in mathematics from Fuzhou University, Fuzhou, China, in 2019. His current research interests include computational intelligence, image processing, system identification, and nonlinear time-series analysis.



**Jia-Li Yin** received the Ph.D. degree in the Department of Computer Science and Engineering, Yuan Ze University, Taoyuan, Taiwan, in 2020. She is currently a Professor and Qishan Scholar with the College of Computer Science and Big Data, Fuzhou University, China. Her research interests include digital image processing, computer vision, pattern recognition, and deep learning.



**C. L. Philip Chen** received the M.S. degree in electrical engineering from the University of Michigan, Ann Arbor, MI, USA, in 1985, and the Ph.D. degree in electrical engineering from Purdue University, West Lafayette, IN, USA, in 1988. He is currently the Dean of the School of Computer Science and Engineering, South China University of Technology, Guangzhou 510641, China. His current research interests include systems, cybernetics, and computational intelligence. Dr. Chen is a Fellow of the AAAS.